SCIENCE CHINA
Earth Sciences

• RESEARCH PAPER •

May 2017 Vol.60 No.5: 866–875
doi: 10.1007/s11430-016-9020-8

Identifying the sensitive area in adaptive observation for predicting the upstream Kuroshio transport variation in a 3-D ocean model

ZHANG Kun[1,2], MU Mu[3] & WANG Qiang[1,4*]

[1] *Key Laboratory of Ocean Circulation and Waves, Institute of Oceanology, Chinese Academy of Sciences, Qingdao 266071, China;*
[2] *University of Chinese Academy of Sciences, Beijing 100049, China;*
[3] *Institute of Atmospheric Sciences, Fudan University, Shanghai 200433, China;*
[4] *Laboratory for Ocean and Climate Dynamics, Qingdao National Laboratory for Marine Science and Technology, Qingdao 266237, China*

Received January 16, 2017; accepted February 20, 2017; published online March 24, 2017

Abstract Using the conditional nonlinear optimal perturbation (CNOP) approach, sensitive areas of adaptive observation for predicting the seasonal reduction of the upstream Kuroshio transport (UKT) were investigated in the Regional Ocean Modeling System (ROMS). The vertically integrated energy scheme was utilized to identify sensitive areas based on two factors: the specific energy scheme and sensitive area size. Totally 27 sensitive areas, characterized by three energy schemes and nine sensitive area sizes, were evaluated. The results show that the total energy (TE) scheme was the most effective because it includes both the kinetic and potential components of CNOP. Generally, larger sensitive areas led to better predictions. The size of 0.5% of the model domain was chosen after balancing the effectiveness and efficiency of adaptive observation. The optimal sensitive area OSen was determined accordingly. Sensitivity experiments on OSen were then conducted, and the following results were obtained: (1) In OSen, initial errors with CNOP or CNOP-like patterns were more likely to yield worse predictions, and the CNOP pattern was the most unstable. (2) Initial errors in OSen rather than in other regions tended to cause larger prediction errors. Therefore, adaptive observation in OSen can be more beneficial for predicting the seasonal reduction of UKT.

Keywords Sensitive area, Adaptive observation, The upstream Kuroshio transport, Conditional nonlinear optimal perturbation (CNOP)

Citation: Zhang K, Mu M, Wang Q. 2017. Identifying the sensitive area in adaptive observation for predicting the upstream Kuroshio transport variation in a 3-D ocean model. Science China Earth Sciences, 60: 866–875, doi: 10.1007/s11430-016-9020-8

1. Introduction

The Kuroshio Current (KC) originates where the North Equatorial Current (NEC) encounters the Philippine coast and bifurcates into the Mindanao Current (MC) and the KC. After flowing along the Taiwan coast, through the East China Sea and past the southern coast of Japan, the KC then flows eastward to form the Kuroshio extension (Nitani, 1972). The upstream Kuroshio generally refers to the KC from the NEC bifurcation to south of Taiwan. As the origin of the subtropical gyre in North Pacific, the variation of the upstream Kuroshio transport (UKT) has considerable influence on climate change, oceanic circulation structures and ecological environments (Hu et al., 2015; Rudnick et al., 2015). Therefore, accurately forecasting variations of UKT is of great significance.

Previous studies have indicated that UKT generally undergoes rapid reduction in autumn (Qiu and Lukas, 1996; Yaremchuk and Qu, 2004; Kang et al., 2011; Qu et al., 1998), hereinafter called the seasonal reduction of UKT. Such seasonal transport reduction may occur for different durations and with different reduction magnitudes, and this considerable variability makes its accurate forecast challenging (Qiu and Lukas, 1996; Yaremchuk and Qu, 2004; Cai et al., 2009;

* Corresponding author (email: wangqiang@qdio.ac.cn)

Kang et al., 2011). As is well known numerical forecast performances are sensitive to the accuracy of initial conditions (ICs; e.g., Mu, 2013; Mu et al., 2015; Majumdar, 2016); reliable ICs are more likely to yield good forecasts. Moreover, recent studies focused on KC predictability have revealed that initial errors can have dramatic influence on forecasting the variation of the KC (Fujii et al., 2008; Wang et al., 2013). Therefore, providing more reliable ICs could be an effective way to improve predictions of the seasonal reduction of UKT.

Observation data assimilation is a common way to obtain better ICs for numerical predictions (e.g., Tang et al., 2004; Onken et al., 2005; Farrara et al., 2013). As field-deployed observations are costly and cannot fully cover the vast space of the forecasted events, observation strategies on guiding where limited observations should be deployed are urgently needed. Adaptive observation (or targeted observation) is one such strategy developed since the 1990s (e.g., Palmer et al., 1998; Langland, 2005), aiming to better predict events by implementing additional observations in specific regions (called sensitive areas). Adaptive observation was first applied in atmospheric fields; therefore, the improved prediction skills for many meteorological applications, such as weather forecast, El Niño-Southern Oscillation (ENSO) forecast and tropical cyclone (TC) forecast, have benefited greatly from this strategy (Morss et al., 2001; Duan and Mu, 2006; Wu et al., 2007; Qin and Mu, 2011; Hu and Duan, 2016). So far, oceanic applications of adaptive observation remain limited (Wang et al., 2013; Li et al., 2014), although such applications are promising to mitigate the greater costs of oceanic field-deployed observations.

A vital issue in adaptive observation is identifying sensitive areas, which are the optimal locations for observation. Multiple strategies for identifying sensitive areas have been developed since the mid-1990s. Some strategies employ the ensemble technique, such as the ensemble transform Kalman filter (Bishop et al., 2001) and the ensemble Kalman filter (Hamill and Snyder, 2002), whereas some employ the adjoint technique, such as with singular vectors (SVs; Palmer et al., 1998), adjoint sensitivities (Ancell and Mass, 2006) and the adjoint-derived sensitivity steering vector (Wu et al., 2007). Recently, Mu et al. (2009) utilized the conditional nonlinear optimal perturbation (CNOP) approach for adaptive observation of the North Pacific typhoon prediction. The CNOP approach is a nonlinear method used to identify the optimal initial error causing the largest prediction error (Mu et al., 2003). Therefore, this approach is able to delineate sensitive areas in nonlinear forecast systems. To date, CNOP has been successfully applied to determine sensitive areas for predicting ENSO (Duan et al., 2004; Yu et al., 2012), TCs (Tan et al., 2010; Qin and Mu, 2011; Zhou and Mu, 2012), the Kuroshio large meander (Wang et al., 2013) and the ocean state of the South China Sea (Li et al., 2014).

Previous studies have indicated that UKT variation is influenced by nonlinear processes at various time-scales, such as ENSO, monsoons and meso-scale eddies (e.g., Qiu and Lukas, 1996; Kim et al., 2004; Lien et al., 2014). Nonlinear CNOP-based adaptive observation therefore is feasible for improving the prediction of UKT variation. The Regional Ocean Modeling System (ROMS) is a widely used 3-D operational model that simulates the KC well (Zhu et al., 2015; Zhang et al., 2016). Therefore, using the ROMS simulation and the CNOP approach, this study is conducted to identify the optimal sensitive area in adaptive observation for predicting the seasonal reduction of UKT.

2. Model and methodology

2.1 Model simulation

We use the ROMS model to simulate the Kuroshio. The ROMS is a 3-D, hydrostatic, free-surface model developed for regional ocean simulation (Song and Haidvogel, 1994). It employs the vertical terrain-following coordinate system and the generalized horizontal orthogonal curvilinear coordinate system and provides a series of horizontal diffusion and vertical mixing parameterization schemes (Shchepetkin and McWilliams, 2003, 2005). For this study, we select harmonic horizontal mixing (Wajsowicz, 1993) and K-profile vertical parameterization (Large et al., 1994). The adjoint model of the ROMS (Moore et al., 2004) is also used with the same settings as the nonlinear model.

The selected model domain is within 0.3°–29°N and 112°–162°E. A resolution of 1/8° and 32 vertical levels are adopted, yielding 400×240×32 grids in total. The topography is interpolated from the worldwide 2-min gridded bathymetry dataset ETOPO2, and these data are then smoothed to avoid large pressure gradients. The initial temperature and salinity in January are interpolated from monthly climatology means of the Simple Ocean Data Assimilation (SODA) 2.2.4 datasets (Carton and Giese, 2008). The initial free-surface elevation and velocity are zero. Surface forcing is derived from monthly climatology data of the Comprehensive Ocean-Atmosphere Data Set (COADS; Diaz et al., 2002). All lateral boundaries are open, with boundary data interpolated from the monthly SODA climatology. Moreover, different boundary conditions are chosen for different variables. Specifically, we adopt the Chapman boundary condition for sea surface height, the Flather boundary condition for barotropic velocity and gradient boundary conditions for 3-D velocity, temperature and salinity (Marchesiello et al., 2001).

The model runs for 40 years, and the output data of the last 25 years are used. The validation of the simulated oceanic currents and UKT variation has been described in Zhang et al. (2016). The results show that the NEC-MC-KC (NMK)

system is successfully reproduced and that the simulated upstream Kuroshio coincides well with both ocean observations and reanalysis. Moreover, the seasonal reduction of UKT is also well simulated, of which UKT is defined as the northward current flowing through the target section S (i.e., the section extending from the Philippine coast to 124°E in the upper 600 m at 18°N).

2.2 CNOP approach and calculation

The CNOP approach and its calculation are briefly described in this subsection. The solution of a nonlinear model is denoted as:

$$\boldsymbol{X}_t = M_t(\boldsymbol{X}_0), \tag{1}$$

where, $\boldsymbol{X}_0$ and $\boldsymbol{X}_t$ are the state vectors at the initial time and the future time t, respectively, and M_t is the propagator of the nonlinear ROMS model used to propagate $\boldsymbol{X}_0$ to $\boldsymbol{X}_t$. If an initial error $\boldsymbol{x}_0$ satisfying the initial condition constraint $\|\boldsymbol{x}_0\|_A \le \delta$ is superimposed on the initial state $\boldsymbol{X}_0$, the following constraint optimization problem exists:

$$J(\boldsymbol{x}_{0\delta}) = \max_{\|\boldsymbol{x}_0\|_A \le \delta} J(\boldsymbol{x}_0) = \max_{\|\boldsymbol{x}_0\|_A \le \delta} \| M_t(\boldsymbol{X}_0 + \boldsymbol{x}_0) - M_t(\boldsymbol{X}_0) \|_B^2, \tag{2}$$

where, $J(\boldsymbol{x}_0)$ is the objective function used to estimate the nonlinear evolution of $\boldsymbol{x}_0$ at the prediction time. The optimal initial error $\boldsymbol{x}_{0\delta}$ that solves eq. (2) is called the CNOP-type initial error or CNOP (Mu et al., 2003).

In practice, the objective function and the initial constraint are defined according to the specific problem addressed. To evaluate the impacts of error evolution on UKT prediction, the objective function is selected as the square of UKT change induced by initial errors, which is expressed as follows:

$$J = \left(\int_S v'_t \mathrm{d}x\mathrm{d}z \right)^2, \tag{3}$$

where, v'_t denotes the meridional velocity anomaly induced by initial errors at forecast time t, and S is the target section.

The initial constraint is selected as total energy (TE, sum of kinetic and potential energy) of the initial errors in the entire domain V (Moore et al., 2003; Fujii et al., 2008), which is expressed as:

$$\| x_0 \|_A^2 = \frac{\rho_{ref}}{2} \left\{ \int_V \left[(u'_0)^2 + (v'_0)^2 + \left(\frac{g\rho'_0}{\rho_{ref} N_0} \right)^2 \right] \mathrm{d}x\mathrm{d}y\mathrm{d}z + g \int_V (\eta'_0)^2 \mathrm{d}x\mathrm{d}y \right\} \le \delta^2, \tag{4}$$

where, g and N_0 are the gravitational acceleration and the Brunt-Väisälä frequency of the ICs, respectively; η'_0, ρ'_0, u'_0 and v'_0 denote the free-surface elevation, density, and the zonal and meridional velocity components of initial errors. The density perturbation is calculated using the linear state equation:

$$\rho = \rho_{ref}(\alpha T + \beta S), \tag{5}$$

where, α=−1.7×10^{-4} kg m^{-3} K^{-1} and β=−1.7×10^{-4} kg m^{-3} psu^{-1} denote the expansion coefficients for temperature and salinity, respectively; ρ=1027 kg m^{-3} is the reference density. The constraint radius δ is set to 5×10^6 J$^{1/2}$, which ensures stable model integration and keeps UKT changes caused by initial errors within an appropriate range.

To compute CNOP, a typical seasonal transport reduction event (the reference state) is chosen. This event lasts for about two months, beginning in August (Model Day 6335) and ending in October (Model Day 6399). The UKT of the reference state undergoes a rapid decrease by approximately 8.0 Sv (1 Sv=10^6 m^3 s^{-1}) during this period. Based on these settings, CNOP is determined using the Spectral Projected Gradient 2 (SPG2) optimization algorithm (Birgin et al., 2000). As described by Zhang et al. (2016), the CNOP-type errors are mainly distributed within 127°–130°E and 16°–18°N horizontally and within the upper 1000 m vertically.

3. Identification of sensitive areas

Previous studies have investigated the impacts of CNOP-based sensitive areas determined by different guidelines in the atmosphere (Tan et al., 2010; Zhou and Zhang, 2014). However, no such studies have been performed for oceanic adaptive observations. In this study, we try to identify the optimal sensitive area in adaptive observation for predicting the seasonal reduction of UKT.

The vertically integrated energy scheme is employed to identify sensitive areas. In this scheme, a sensitive area is defined as the horizontal grids where the CNOP-type errors have vertically integrated energy larger than a certain value ε. In practice, ε can be adjusted to obtain sensitive areas of different sizes. The depth range chosen for integrating energy is the upper 1000 m, where the CNOP-type errors are mainly located. The identified sensitive area therefore can reflect the general distribution of CNOP-type errors. This scheme has been demonstrated to be effective for adaptive observations of typhoons (Zhou and Zhang, 2014). Of further interest, we will examine whether this scheme is effective for oceanic adaptive observations.

To determine the sensitive area, two guidelines should be decided: the specific energy scheme and the sensitive area size. As described in subsection 2.2, the initial constraint is defined as TE of initial errors, including kinetic energy (KE) and potential energy (PE). To find the most effective energy scheme, sensitive areas determined based on three energy schemes (KE, PE and TE schemes) are investigated. The spatial distributions of the vertically integrated KE, PE and TE of CNOP are first compared (Figure 1). KE values are much smaller than PE values; therefore, the spatial pattern of TE is mainly determined by the distribution of PE. Moreover, the grids with larger KE values are located more east compared

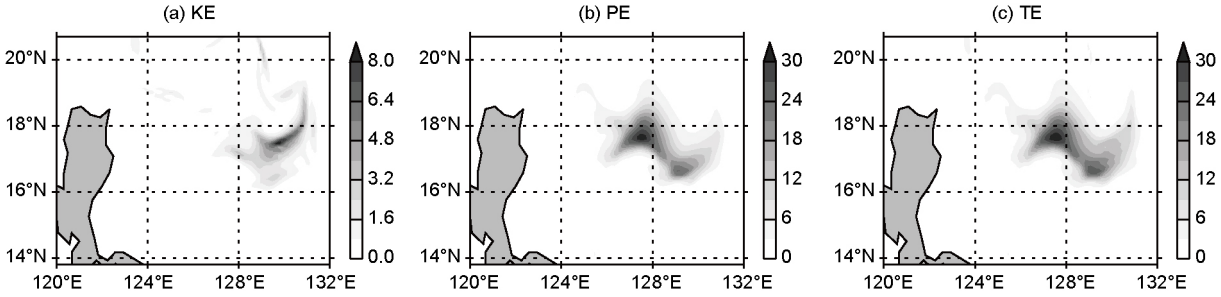

Figure 1 Distributions of non-dimensional vertically integrated energy of CNOP in the upper 1000 m.

to the grids of larger PE or TE values. Consequently, the sensitive areas determined based on the TE and PE (TE) energy schemes differ considerably, and adaptive observations based on these sensitive areas may affect UKT predictions quite differently. In addition, adaptive observations within larger sensitive areas generally bring greater improvements of forecast skills. However, the costs and difficulties of conducting targeted observations increase rapidly with enlarging sensitive areas. Therefore, it is practical to assess how enlarging the sensitive area will improve the forecast of interest. As noted above, the sensitivity of the sensitive areas, which generally refers to whether the ICs in the sensitive areas are sensitive to UKT variation, is affected by both the specific energy scheme and the sensitive area size.

To select the appropriate energy scheme and sensitive area size, the following experiments are conducted. Totally 27 different sensitive areas are identified. These sensitive areas are characterized by three energy schemes and nine sensitive area sizes (linearly increasing from 0.1% to 0.9% of the model domain), which are correspondingly denoted as Sen_KE_1 to Sen_KE_9, Sen_PE_1 to Sen_PE_9 and Sen_TE_1 to Sen_TE_9. To illustrate the distributions of these sensitive areas, snapshots of selected examples are provided in Figure 2. The sensitive areas determined using the PE scheme (denoted as Sen_PEs) are similar to those determined using the TE scheme (denoted as Sen_TEs), whereas the sensitive areas determined using the KE scheme (denoted as Sen_KEs) differ considerably. For instance, Sen_KE_3 differs greatly from Sen_PE_3 and Sen_TE_3 in that most of the former is located east of 129°E. However, Sen_KEs become more similar to Sen_PEs or Sen_TEs as the size of the sensitive area grows. As shown in the third row of Figure 2, the sensitive areas determined by KE and PE are quite similar. To quantitatively compare these sensitive areas, Figure 3 demonstrates the percentages of grids shared between Sen_KEs, Sen_PEs and Sen_TEs. The percentages of shared grids between Sen_PEs and Sen_TEs all exceed 80.0%. In contrast, the percentages of grids shared between Sen_KEs and both Sen_PEs and Sen_TEs are lower, especially with small sensitive areas. In particular, the percentage of grids shared between Sen_PE_1 and Sen_KE_1 is zero, which indicates that the two sensitive areas are completely different. These percentages become larger as the sensitive area size grows, and reach approximately 60% for the largest sensitive area size.

Ideal hindcasting experiments are conducted to assess the effectiveness of the identified sensitive areas. Here, "ideal" means that the model is perfect without model error and that all prediction errors are induced by uncertainty of ICs. Therefore, ideal hindcasting experiments can be conducted to evaluate the effects of directly removing initial errors within the sensitive areas, and are performed as follows. First, 27 initial errors are generated by removing the CNOP-type errors in the upper 1000 m of the identified sensitive areas. Subsequently, each of these initial errors is superimposed onto the initial reference state, and the nonlinear model is integrated for 64 days. The UKT changes at the prediction time caused by the initial errors are used to denote the corresponding prediction errors. The prediction benefits by removing the CNOP-type errors in each sensitive area are estimated using the following ratio:

$$k = \frac{T_{\mathrm{CNOP}} - T_i}{T_{\mathrm{CNOP}}}, \tag{6}$$

where, T_{CNOP} and T_i (i=1, 2, 3,…, 27) denote the absolute UKT changes at the prediction time induced by superimposing CNOP and the generated initial errors, respectively.

Figure 4a demonstrates the prediction benefits of these ideal hindcasting experiments. Removing the CNOP-type errors in the identified sensitive areas all improve the prediction of the seasonal reduction of UKT. In particular, when the sensitive area sizes are small (i.e., less than 0.3%), prediction improvements from removing the CNOP-type errors in Sen_KEs are larger than those in Sen_PEs. Recalling that Sen_KEs differ a lot with Sen_PEs in this circumstance, these findings suggest that the sensitive areas determined by the KE scheme are effective even though vertically integrated KE values are much smaller. Therefore, the kinetic components of initial errors cannot be neglected. As the sensitive area size grows, the prediction benefits from removing the CNOP-type errors in Sen_PEs increase more rapidly and become larger than those in Sen_KEs, which indicates that the potential components of CNOP also cannot be ignored. Moreover, removing the CNOP-type errors in Sen_TEs generally yields the best pre-

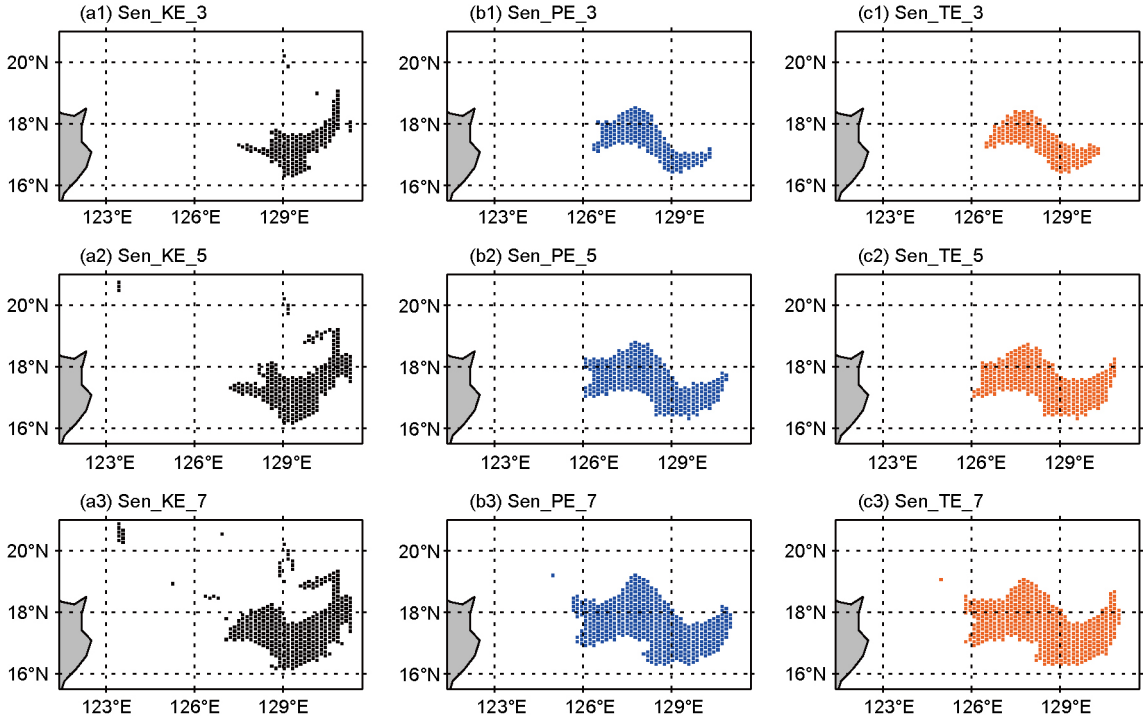

Figure 2 Snapshots of selected sensitive areas determined by different energy schemes and sensitive area sizes; (a1)–(a3) denote the sensitive areas determined using the KE scheme and horizontal sizes of 0.3%, 0.5% and 0.7% of the model domain, respectively. Similarly, (b1)–(b3) and (c1)–(c3) denote the sensitive areas determined using the PE and TE schemes, respectively.

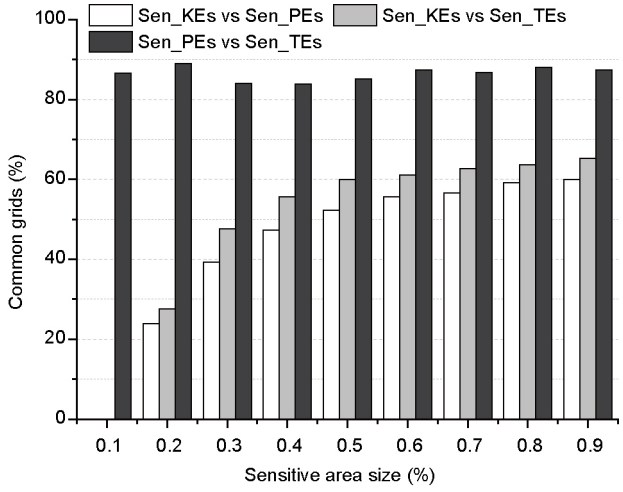

Figure 3 Percentages of grids shared by Sen_KEs, Sen_PEs and Sen_TEs for different sensitive area sizes.

diction for all investigated sensitive area sizes. The reason could be that the TE scheme accounts for the impacts of both the kinetic and potential components of initial errors at the same time. Therefore, the TE scheme is identified as the most effective energy scheme for identification of sensitive areas.

Another issue to be resolved is choosing the appropriate sensitive area size. As shown in Figure 4a, removing CNOP-type errors in larger sensitive areas indeed leads to higher prediction benefits. The largest sensitive area size is the best if only the prediction skill improvement is considered. However, we must also consider the difficulties and economic costs associated with deploying observations over larger sensitive areas. Therefore, the optimal sensitive area is one that results in considerable prediction improvement with relatively high efficiency. To explore the efficiency of different sensitive area sizes, prediction benefit increments by enlarging Sen_TEs from 0.1% to 0.9% are investigated (shown in Figure 4b). The prediction benefit increments induced by increasing the Sen_TE size by 0.1% are much larger when sensitive areas are smaller, and the opposite is also true. For instance, enlarging the Sen_TE size by 0.1% can induce acceptable benefit increments greater than 5% when the size is smaller than 0.5%. For Sen_TEs larger than 0.5%, the effects of enlarging Sen_TEs on prediction skill improvement are limited. In this case, performing ideal hindcasting experiments is less efficient. The reason could be that the grids in the enlarged sensitive areas in this circumstance are relatively less effective for improving UKT prediction because we prefer to choose grids with greater integrated energy for smaller sensitive areas. In fact, the objective is to obtain considerable prediction improvements with a relatively small sensitive area. After balancing the effectiveness and efficiency of different Sen_TEs, the sensitive area size of 0.5% of the model domain is selected.

Ultimately, the TE scheme and the sensitive area size of 0.5% of the model domain are found to be most suitable. The

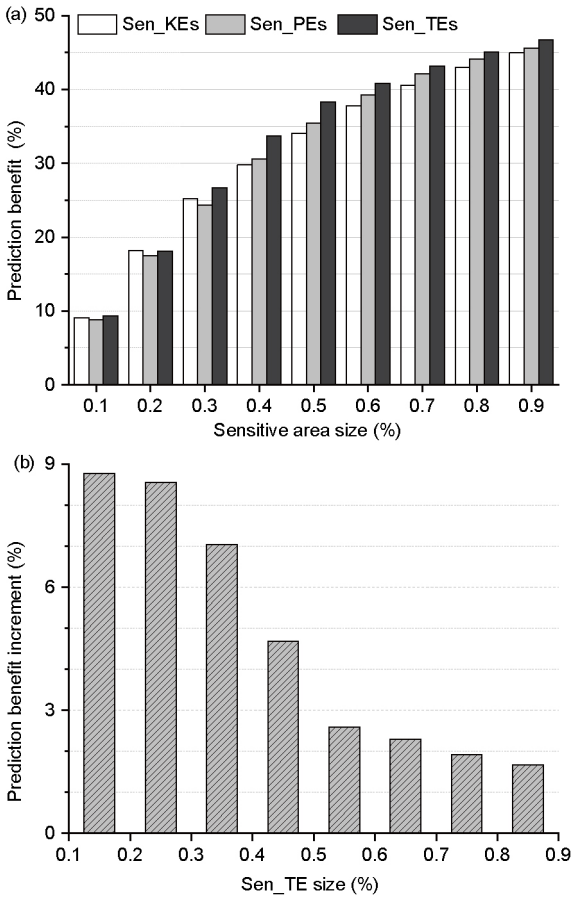

Figure 4 (a) Prediction benefits of performing ideal hindcasting experiments in identified sensitive areas, (b) prediction benefit increments of enlarging Sen_TEs from 0.1% to 0.9%.

optimal sensitive area determined by the two guidelines is denoted as OSen (i.e., Sen_TE_5, stippled in Figure 5). OSen covers the large-amplitude region of the vertically integrated TE of CNOP. The ideal hindcasting experiment performed in OSen can improve UKT prediction by approximately 40%.

4. Sensitivity experiments

In this section, we examine whether UKT forecasts are sensitive to the initial errors in OSen. The following sensitivity experiments are conducted to investigate the impacts of the spatial patterns and locations of initial errors.

4.1 Impacts of spatial patterns of initial errors

First, the CNOP-OSen initial error and 30 groups of random initial errors are generated. CNOP-OSen is produced by only retaining the CNOP-type errors in the upper 1000 m of OSen. For the 30 random initial errors, all variables are zero except those located in the upper 1000 m of OSen, which are set to random numbers. The random number at each grid is stochastically selected from a matrix satisfying the normal distribution $N(0, \sigma_1)$, where σ_1 is randomly chosen from 0 to 2. For

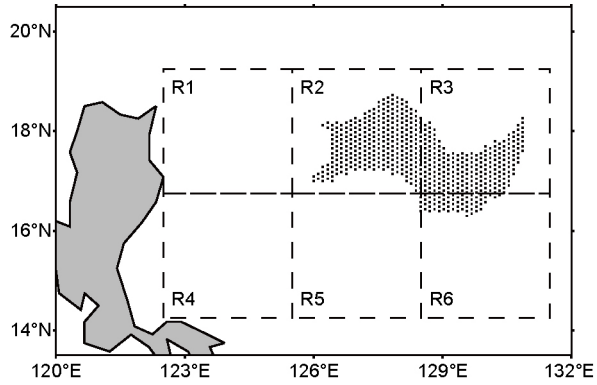

Figure 5 Domains of the compared areas (R1 to R6). The dotted region denotes the identified sensitive area OSen.

fair comparison, all random initial errors have been scaled to ensure that their total energy equals that of CNOP-OSen. We then superimpose CNOP-OSen and the 30 random initial errors on the initial reference state and integrate the nonlinear model for 64 days, respectively.

The UKT changes caused by these errors at the prediction time t are then investigated. The results indicate that superimposing CNOP-OSen leads to a UKT increase of 1.47×10^6 $m^3\ s^{-1}$. However, the UKT changes caused by the random initial errors are much smaller (shown in Figure 6), and are highly random; among the 30 groups of the random errors, half lead to increased UKT, whereas the other half cause UKT decrease. Some random errors cause prediction errors greater than 20000 $m^3\ s^{-1}$, whereas some barely affect the UKT prediction. Statistics of the absolute changes in UKT induced by these random errors are listed in Table 1. The mean absolute UKT change caused by all random errors is 7736 $m^3\ s^{-1}$, which accounts for only 0.6% of the UKT change induced by CNOP-OSen. The only difference between CNOP-OSen and the random initial errors is whether these errors have the CNOP-type spatial pattern. Therefore, it can be inferred that the spatial patterns of initial errors play an important role in error growth and that initial errors with CNOP or CNOP-like patterns are more likely to cause large prediction errors.

To examine the relationships between the spatial patterns of initial errors and the prediction errors they cause, correlation coefficients between CNOP-OSen and these random initial errors have been calculated. As depicted in Figure 7a, the random initial errors show different correlations with CNOP-OSen, although all correlation coefficients are small. The random initial errors with stronger correlations (whether positive or negative) with CNOP-OSen tend to cause larger prediction errors. These findings support the speculation that initial errors with CNOP-like patterns are likely to cause poorer predictions. However, this possibly is not convincingly demonstrated by these correlations because the correlation coefficients between CNOP-OSen and the random initial errors are very small.

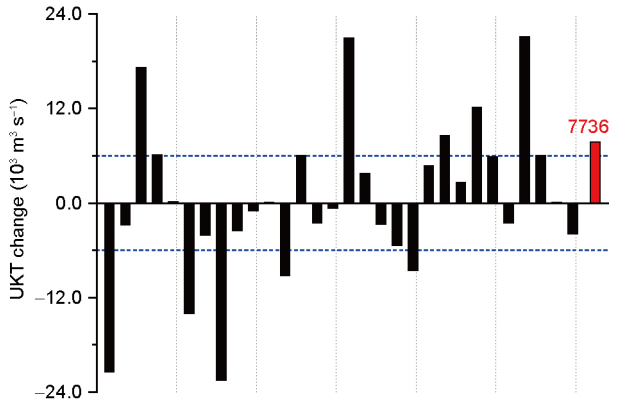

Figure 6 The UKT changes at the prediction time caused by the random initial errors in OSen. The red column denotes the mean of the absolute UKT changes. The dashed lines denote UKT changes of 6000 and −6000 m^3 s^{-1}.

Table 1 Statistics of the absolute UKT changes caused by random initial errors in OSen and the compared areas (R1 to R6)

Area	Number of random errors (m^3 s^{-1})	Maximum (m^3 s^{-1})	Mean (m^3 s^{-1})	Median (m^3 s^{-1})
OSen	30	22483	7736	5046
R1	30	5594	2090	2196
R2	30	16247	4186	3279
R3	30	15416	4458	4285
R4	30	3742	1596	1473
R5	30	6094	2179	2092
R6	30	9882	3552	2851
Mean of all random initial errors in R1–R6			3010	

To confirm this hypothesis, the following experiments are performed. A total of 30 special-pattern initial errors are generated, whose correlation coefficients with CNOP-OSen range from −1.0 to 1.0. For each special-pattern error, all variables are zero except for those in the upper 1000 m of OSen, which are set to specific numbers. The specific number at a particular grid is generated as follows:

$$\eta = \pm(\eta_{\mathrm{CNOP}} + \eta_{\mathrm{ran}}), \tag{7}$$

where, η is the desired specific number and η_{CNOP} is the value of the CNOP-type error; η_{ran} is stochastically chosen from a matrix satisfying normal distribution $N(\mu_2, \sigma_2)$. For different special-pattern errors, μ_2 and σ_2 are differently chosen to ensure that the correlation coefficients extend from −1.0 to 1.0. For fair comparison, the special-pattern errors are also scaled to have same total energy as CNOP-OSen. The impacts of these errors on UKT prediction are also investigated. Figure 7b displays a scatter plot of the correlation coefficients between CNOP-OSen with the special-pattern errors and the induced UKT changes. The UKT changes caused by the special-pattern initial errors are much larger than those caused by the random initial errors. The mean absolute UKT change induced by the special-pattern errors is about 70 times larger than that induced by the random initial errors. Furthermore, stronger correlations between the special-pattern errors and CNOP-OSen correspond to greater prediction errors. These findings not only reflect the important role of spatial patterns in error growth, but also emphasize that the CNOP pattern may be the most unstable error pattern.

4.2 Impacts of locations of initial errors

To explore the impacts of the locations of initial errors, six areas (denoted as R1, R2, R3, R4, R5 and R6; see Figure 5) with the same size as OSen are selected for comparison. All compared areas are located in east or south of the target section S, where initial errors have important impacts on UKT variation (Rudnick et al., 2015). For each compared area, a similar method to that described in subsection 4.1 to generate random initial errors is used to generate 30 groups of random initial errors. The random initial errors for each compared area only occur in the upper 1000 m of R1–R6 accordingly. We then superimpose these random initial errors onto the initial reference state and investigate the UKT changes induced by these errors at the prediction time.

Figure 8 demonstrates the UKT changes induced by the random initial errors in each compared area. The prediction errors caused by the random errors of all compared areas show large uncertainties. Some random initial errors cause clear UKT changes, whereas some barely affect UKT variation. Some errors cause the UKT to increase, whereas others cause it to decrease. Although the uncertainties exist, two findings are notable. First, the absolute UKT changes caused by the random errors in all compared areas are much smaller than those caused by the random errors in OSen. Nearly half of the random initial errors (15 groups) in OSen cause UKT to change by more than 6000 m^3 s^{-1}. However, the numbers of initial errors that cause such large changes of UKT in R1–R6 are small, with a maximum of 7 (in R3) and a minimum of zero (in R1 and R4). The red columns denoting the mean absolute UKT changes in Figures 6 and 8 reflect this finding more directly. Secondly, the UKT changes caused by the random initial errors in R2 and R3 are comparatively larger. The mean absolute UKT changes in R2 and R3 are about twice as large as those in R1, R4 and R5.

Further statistics of the absolute UKT changes caused by the random initial errors in OSen and R1–R6 are listed in Table 1. All values related to the absolute UKT changes (including maxima, means and medians) in OSen are much larger than those in any region from R1 to R6. The mean absolute UKT change induced by the random initial errors in all compared areas is 3010 m^3 s^{-1}, which is 38% of that caused by the random initial errors in OSen. For the mean absolute UKT changes caused by the random errors in the compared areas,

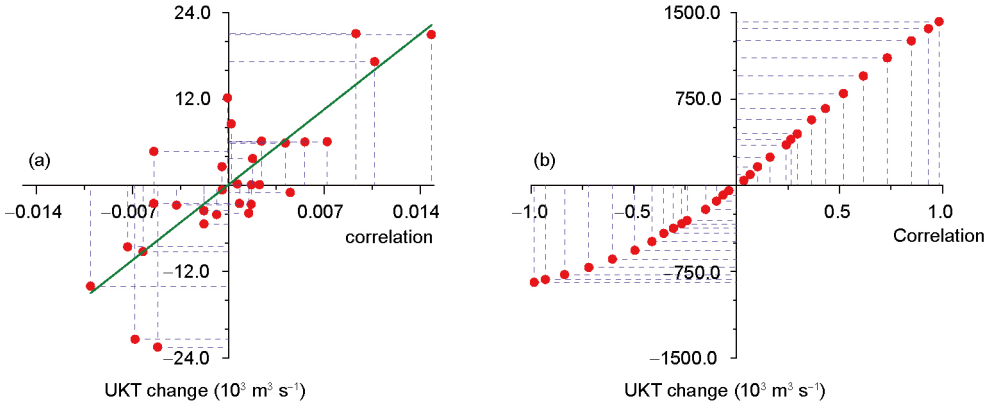

Figure 7 Scatter diagrams of UKT changes and the correlation coefficients between CNOP-OSen and initial errors in OSen: (a) for random initial errors and (b) for special-pattern initial errors. The green line is the regression line.

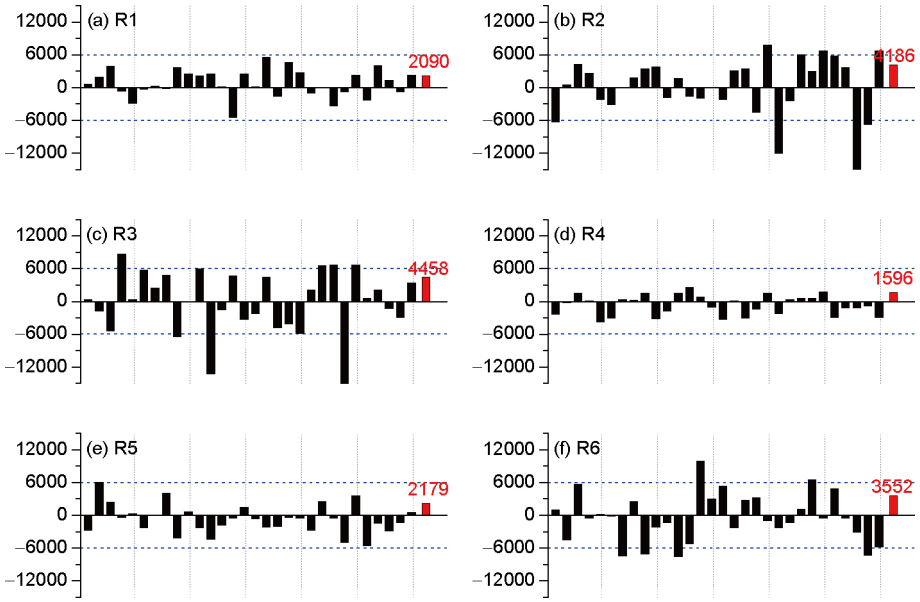

Figure 8 The UKT changes (unit: $m^3 s^{-1}$) at the prediction time caused by the random initial errors in each compared areas (R1 to R6). The red column denotes the mean of the absolute UKT changes. The dashed lines denote UKT changes of 6000 and −6000 $m^3 s^{-1}$.

the largest (4458 $m^3 s^{-1}$) and smallest (1596 $m^3 s^{-1}$) occur in R3 and R4, accounting for about 57% and 21% of that in OSen (7736 $m^3 s^{-1}$). In addition, the statistical data for R2 and R3 are indeed greater. The reason for this difference is that R2 and R3 share more grids with OSen than R1, R4 and R5 (as shown in Figure 5). In fact, calculations indicate that OSen primarily overlaps with R2 and R3, with common grid percentages of 49.8% and 36.9%, respectively.

Because all random initial errors in OSen and the compared areas are randomly generated, the reason for such different results is inferred to be the locations of the initial errors. Considering that the random errors in OSen generally lead to poorer predictions, OSen is interpreted to be more sensitive to the growth of initial errors. Moreover, the fact that initial errors in areas that share more grids with OSen lead to larger prediction errors also emphasizes the sensitivity of the location of OSen.

5. Discussion and summary

With the ROMS model, UKT variations, especially the seasonal reduction, were successfully simulated. Using the CNOP approach, the optimal sensitive area in adaptive observation for predicting a typical transport reduction event was identified. We employed the vertically integrated energy scheme to identify CNOP-based sensitive areas, mainly considering two factors: the specific energy scheme and the sensitive area size. Totally 27 sensitive areas characterized by three energy schemes (KE, PE and TE schemes) and nine sensitive area sizes (linearly increasing from 0.1% to 0.9% of the model domain) were investigated. We performed ideal hindcasting experiments to evaluate the effectiveness of these sensitive areas. The results show that neither the kinetic nor the potential components of CNOP can be neglected. In detail, Sen_KEs are more effective than Sen_PEs for smaller

sensitive areas, and the opposite is true for larger sensitive areas. Moreover, correcting ICs in Sen_TEs tends to yield the greatest benefits. The cause of the sensitivity difference between Sen_KEs and Sen_PEs remains unclear, and thus requires further investigation. The TE scheme was ultimately adopted because it accounts for both the kinetic and potential components. In addition, larger sensitive areas indeed lead to better predictions, but require more observations. After balancing the prediction improvement and loss of efficiency associated with enlarging the sensitive area, the horizontal size of 0.5% of the model domain was selected. Thus, the optimal sensitive area OSen was identified.

Subsequently, sensitivity experiments on OSen were conducted to explore the impacts of the spatial patterns and locations of initial errors. The results show that the initial errors in OSen with CNOP or CNOP-like patterns tend to cause larger prediction errors. Generally, the stronger the correlation between the initial error and CNOP, the worse the resulting prediction is. Therefore, the CNOP pattern could be the most unstable pattern. In addition, initial errors within OSen are more likely to result in poorer predictions than those in other regions. Meanwhile, the prediction errors caused by initial errors in the areas that share more grids with OSen are generally larger. Therefore, reduction of initial errors in the CNOP-determined sensitive area or nearby areas could be more effective for improving the prediction of the seasonal reduction of UKT.

Previous studies have suggested that the westward-propagating eddies can affect UKT variation (Hu et al., 2013; Lien et al., 2014). In fact, the identified OSen is located in the eddy-energetic region formed by the North Pacific Subtropical Countercurrent and the NEC (Qiu, 1999). Oceanic instabilities in this region, mainly baroclinic instability, could cause rapid growth of initial errors and thus result in poor predictions of UKT variation (Qiu, 1999; Chang and Oey, 2014; Zhang et al., 2016). Therefore, conducting additional observations in OSen is expected to be effective for improving the prediction of UKT variation. In addition to the uncertainty of ICs, external forcing, such as wind forcing, also affects the prediction of UKT. Previous studies have shown that the NMK current system is driven by large-scale wind forcing (e.g., Qiu and Lukas, 1996; Qu and Lukas, 2003; Chen and Wu, 2011; Hu and Duan, 2016). Wind forcing can affect the latitude of NEC bifurcation, which could further affect UKT variation by modulating the volume distribution between the tropical gyre and the subtropical gyre. Therefore, the impacts of wind forcing on UKT prediction are worth exploring next.

This study is the first attempt to discuss the guidelines for identifying the CNOP-based sensitive area in a 3-D operational ocean model. This work is preliminary; only the prediction benefits of removing CNOP errors in sensitive areas for a single transport reduction event were examined. Therefore, additional case studies and realistic observation system simulation experiments (OSSEs) will be conducted in the future, with appropriate observation platform designs and data assimilation systems taken into consideration at the same time. Based on this preliminary work, we plan to design the observation network for predicting the seasonal reduction of UKT in the future. We expect that real-time targeted observations will benefit from these results.

Acknowledgements *The authors are grateful to the two anonymous reviewers for their valuable comments and constructive suggestions. This research was supported by the Strategic Priority Research Program of the Chinese Academy of Sciences (Grant No. XDA11010303), the National Natural Science Foundation of China (Grant Nos. 41230420, 41306023 & 41421005) and the National Natural Science Foundation of China-Shandong Joint Fund for Marine Science Research Centers (Grant No. U1406401). The authors gratefully acknowledge the support of K. C. Wong Foundation.*

References

Ancell B C, Mass C F. 2006. Structure, growth rates, and tangent linear accuracy of adjoint sensitivities with respect to horizontal and vertical resolution. Mon Weather Rev, 134: 2971–2988

Birgin E G, Martínez J M, Raydan M. 2000. Nonmonotone spectral projected gradient methods on convex sets. SIAM J Optim, 10: 1196–1211

Bishop C H, Etherton B J, Majumdar S J. 2001. Adaptive sampling with the ensemble transform Kalman filter. Part I: Theoretical aspects. Mon Weather Rev, 129: 420–436

Cai, R S, Zhang Q L, Qi Q H. 2009. Characters of transport variations at the source and adjacent area of Kuroshio (in Chinese with English abstract). J Oceanogr Taiwan Strait, 28: 299–306

Carton J A, Giese B S. 2008. A reanalysis of ocean climate using simple ocean data assimilation (SODA). Mon Weather Rev, 136: 2999–3017

Chang Y L, Oey L Y. 2014. Analysis of STCC eddies using the Okubo-Weiss parameter on model and satellite data. Ocean Dyn, 64: 259–271

Chen Z, Wu L. 2011. Dynamics of the seasonal variation of the North Equatorial Current bifurcation. J Geophys Res, 116: C02018

Diaz H, Folland C, Manabe T, Parker D, Reynolds R, Woodruff S. 2002. Workshop on advances in the use of historical marine climate data. Bull World Meteorol Organ, 51: 377–379

Duan W S, Mu M. 2006. Investigating decadal variability of El Nino-southern oscillation asymmetry by conditional nonlinear optimal perturbation. J Geophys Res, 111: C07015

Duan W S, Mu M, Wang B. 2004. Conditional nonlinear optimal perturbations as the optimal precursors for El Nino-southern oscillation events. J Geophys Res, 109: D23105

Farrara J D, Chao Y, Li Z, Wang X, Jin X, Zhang H, Li P, Vu Q, Olsson P Q, Schoch G C, Halverson M, Moline M A, Ohlmann C, Johnson M, McWilliams J C, Colas F A. 2013. A data-assimilative ocean forecasting system for the Prince William sound and an evaluation of its performance during sound Predictions 2009. Cont Shelf Res, 63: S193–S208

Fujii Y, Tsujino H, Usui N, Nakano H, Kamachi M. 2008. Application of singular vector analysis to the Kuroshio large meander. J Geophys Res, 113: C07026

Hamill T M, Snyder C. 2002. Using improved Background-Error covariances from an ensemble Kalman filter for adaptive observations. Mon Weather Rev, 130: 1552–1572

Hu D X, Hu S J, Wu L X, Li L, Zhang L L, Diao X Y, Chen Z H, Li Y L, Wang F, Yuan D L. 2013. Direct measurements of the Luzon Undercurrent. J Phys Oceanogr, 43: 1417–1425

Hu D X, Wu L X, Cai W J, Gupta A S, Ganachaud A, Qiu B, Gordon A L, Lin X P, Chen Z H, Hu S J, Wang G J, Wang Q Y, Sprintall J, Qu T

D, Kashino Y, Wang F, Kessler W S. 2015. Pacific western boundary currents and their roles in climate. Nature, 522: 299–308
Hu J T, Duan W S. 2016. Relationship between optimal precursory disturbances and optimally growing initial errors associated with ENSO events: Implications to target observations for ENSO prediction. J Geophys Res-Oceans, 121: 2901–2917
Kang L, Wang F, Chen Y L. 2011. Characteristics of temporal and spatial distribution of North Pacific low-lalitude Western Boundary Currents (in Chinese with English abstract). Mar Forecasts, 28: 32–39
Kim Y Y, Qu T, Jensen T, Miyama T, Mitsudera H, Kang H W, Ishida A. 2004. Seasonal and interannual variations of the North Equatorial Current bifurcation in a high-resolution OGCM. J Geophys Res, 109: C03040
Langland R H. 2005. Issues in targeted observing. Q J R Meteorol Soc, 131: 3409–3425
Large W G, McWilliams J C, Doney S C. 1994. Oceanic vertical mixing: A review and a model with a nonlocal boundary layer parameterization. Rev Geophys, 32: 363–403
Li Y N, Peng S Q, Liu D L. 2014. Adaptive observation in the South China Sea using CNOP approach based on a 3-D ocean circulation model and its adjoint model. J Geophys Res-Oceans, 119: 8973–8986
Lien R C, Ma B, Cheng Y H, Ho C R, Qiu B, Lee C M, Chang M H. 2014. Modulation of Kuroshio transport by mesoscale eddies at the Luzon Strait entrance. J Geophys Res-Oceans, 119: 2129–2142
Majumdar S J. 2016. A review of targeted observations. Bull Amer Meteorol Soc, 97: 2287–2303
Marchesiello P, McWilliams J C, Shchepetkin A. 2001. Open boundary conditions for long-term integration of regional oceanic models. Ocean Model, 3: 1–20
Moore A M, Arango H G, Di Lorenzo E, Cornuelle B D, Miller A J, Neilson D J. 2004. A comprehensive ocean prediction and analysis system based on the tangent linear and adjoint of a regional ocean model. Ocean Model, 7: 227–258
Moore A M, Vialard J, Weaver A T, Anderson D L T, Kleeman R, Johnson J R. 2003. The role of air-sea interaction in controlling the optimal perturbations of low-frequency tropical coupled ocean-atmosphere modes. J Clim, 16: 951–968
Morss R E, Emanuel K A, Snyder C. 2001. Idealized adaptive observation strategies for improving numerical weather prediction. J Atmos Sci, 58: 210–232
Mu M. 2013. Methods, current status, and prospect of targeted observation. Sci China Earth Sci, 56: 1997–2005
Mu M, Duan W S, Chen D K, Yu W D. 2015. Target observations for improving initialization of high-impact ocean-atmospheric environmental events forecasting. Nat Sci Rev, 2: 226–236
Mu M, Duan W S, Wang B. 2003. Conditional nonlinear optimal perturbation and its applications. Nonlin Processes Geophys, 10: 493–501
Mu M, Zhou F F, Wang H L. 2009. A method for identifying the sensitive areas in targeted observations for tropical cyclone prediction: Conditional nonlinear optimal perturbation. Mon Weather Rev, 137: 1623–1639
Nitani H. 1972. Beginning of the Kuroshio. In: Stommel H, Yoshida K, eds. Kuroshio: Its Physical Aspects. Tokyo: Univerisity of Tokyo Press. 129–163
Onken R, Robinson A R, Kantha L, Lozano C J, Haley P J, Carniel S. 2005. A rapid response nowcast/forecast system using multiply nested ocean models and distributed data systems. J Mar Syst, 56: 45–66
Palmer T N, Gelaro R, Barkmeijer J, Buizza R. 1998. Singular vectors, metrics, and adaptive observations. J Atmos Sci, 55: 633–653
Qin X H, Mu M. 2011. A study on the reduction of forecast error variance by three adaptive observation approaches for tropical cyclone prediction. Mon Weather Rev, 139: 2218–2232
Qiu B. 1999. Seasonal eddy field modulation of the North Pacific subtropical countercurrent: TOPEX/Poseidon observations and theory. J Phys Oceanogr, 29: 2471–2486
Qiu B, Lukas R. 1996. Seasonal and interannual variability of the North Equatorial Current, the Mindanao Current, and the Kuroshio along the Pacific western boundary. J Geophys Res, 101: 12315–12330
Qu T, Lukas R. 2003. The bifurcation of the North Equatorial current in the Pacific. J Phys Oceanogr, 33: 5–18
Qu T, Mitsudera H, Yamagata T. 1998. On the western boundary currents in the Philippine Sea. J Geophys Res, 103: 7537–7548
Rudnick D L, Jan S, Lee C M. 2015. A new look at circulation in the Western North Pacific. Oceanography, 28: 16–23
Shchepetkin A F, McWilliams J C. 2003. A method for computing horizontal pressure-gradient force in an oceanic model with a nonaligned vertical coordinate. J Geophys Res, 108: 3090
Shchepetkin A F, McWilliams J C. 2005. The regional oceanic modeling system (ROMS): A split-explicit, free-surface, topography-following-coordinate oceanic model. Ocean Model, 9: 347–404
Song Y, Haidvogel D. 1994. A semi-implicit ocean circulation model using a generalized topography-following coordinate system. J Comp Phys, 115: 228–244
Tan X W, Wang B, Wang D L. 2010. Impact of different guidances on sensitive areas of targeting observations based on the CNOP method. J Meteorol Res, 24: 17–30
Tang Y M, Kleeman R, Moore A M. 2004. SST assimilation experiments in a tropical Pacific Ocean model. J Phys Oceanogr, 34: 623–642
Wajsowicz R C. 1993. A consistent formulation of the anisotropic stress tensor for use in models of the large-scale ocean circulation. J Comp Phys, 105: 333–338
Wang Q, Mu M, Dijkstra H A. 2013. The similarity between optimal precursor and optimally growing initial error in prediction of Kuroshio large meander and its application to targeted observation. J Geophys Res-Oceans, 118: 869–884
Wu C C, Chen J H, Lin P H, Chou K H. 2007. Targeted observations of tropical cyclone movement based on the adjoint-derived sensitivity steering vector. J Atmos Sci, 64: 2611–2626
Yaremchuk M, Qu T. 2004. Seasonal variability of the large-scale currents near the coast of the Philippines. J Phys Oceanogr, 34: 844–855
Yu Y, Mu M, Duan W, Gong T. 2012. Contribution of the location and spatial pattern of initial error to uncertainties in El Niño predictions. J Geophys Res, 117: C06018
Zhang K, Wang Q, Mu M, Liang P. 2016. Effects of optimal initial errors on predicting the seasonal reduction of the upstream Kuroshio transport. Deep-Sea Res Part I-Oceanogr Res Pap, 116: 220–235
Zhou F F, Mu M. 2012. The impact of horizontal resolution on the CNOP and on its identified sensitive areas for tropical cyclone predictions. Adv Atmos Sci, 29: 36–46
Zhou F, Zhang H. 2014. Study of the schemes based on CNOP method to identify sensitive areas for typhoon targeted observations (in Chinese with English abstract). Chin J Atmos Sci, 38: 261–272
Zhu X M, Liu G M, Wang J, Wang H, Bao X W, Hu W. 2015. A numerical study on the relationships of the variations of volume transport around the China seas. J Mar Syst, 145: 15–36